Determination of biphasic core–shell droplet properties using aerosol optical tweezers

Kyle Gorkowski,[1] Neil M. Donahue,[1] Ryan C. Sullivan[1*]

[1]Center for Atmospheric Particle Studies, Carnegie Mellon University, Pittsburgh, PA

[*]Corresponding Author: Ryan C. Sullivan; rsullivan@cmu.edu

Abstract

We present a new algorithm for the analysis of whispering gallery modes (WGMs) found in the cavity enhanced Raman spectra retrieved from optically tweezed droplets. Our algorithm improves the computational scaling when analyzing core–shell droplets (i.e. phase-separated or biphasic droplets) in the aerosol optical tweezers (AOT), making it computationally practical to analyze spectra collected at a few Hz over hours-long experiments. This enables the determination of the size and refractive index of both the core and shell phases with high accuracy, at 0.5 Hz time resolution. Phase-separated core–shell droplets are common morphologies in a wide variety of biophysical, colloidal, and aerosolized chemical systems, and have recently become a major focus in understanding the atmospheric chemistry of particulate matter. Our new approach reduces the number of parameters directly searched for, decreasing computational demands. We assess the accuracy of the diameters and refractive indices retrieved from a homogeneous or core–shell droplet. We demonstrate the performance of the new algorithm using experimental data from a droplet of aqueous glycerol coated by squalane. We demonstrate that a shell formation causes adjacent WGMs to split from each other in their wavenumber position through the addition of a secondary organic aerosol shell around a NaCl(aq) droplet. Our new algorithm paves the way for more in-depth physiochemical experiments into liquid–liquid phase separation and their consequences for interfacial chemistry—a topic with growing experimental needs for understanding the dynamics and chemistry of atmospheric aerosol particles, and in biochemical systems.

1. Introduction

Liquid–liquid phase separation is an important phenomenon in many areas of chemistry and biology due to the unique properties that result after phase separation. In biochemistry, liquid–liquid phase separation (LLPS) can be used as a purification or extraction process for biomolecules such as proteins, enzymes, and viruses.[1–7] The concentration of solutes resulting from LLPS can lead to the sequestering of toxic molecules or enhanced reaction rates.[8] In the environment, LLPS can dramatically change the near-surface concentrations of species, either enhancing or reducing their availability for multiphase chemistry.[3,9] For these reasons, accurate and direct measurements of LLPS an important observational need in biochemistry, environmental chemistry, and atmospheric chemistry. This work uses the aerosol optical tweezers to probe LLPS of atmospheric aerosols, but the new analysis method presented is not limited to atmospheric systems.

The aerosol optical tweezers (AOT) has become a valuable technique to directly determine key physicochemical properties of individual aerosols including viscosity, diffusion coefficients, surface tension, morphology, optical properties, hygroscopic growth factors, phase transitions, and heterogeneous chemical reactivity.[10–31] In a typical AOT system, a droplet is optically trapped by a focused laser beam, which also induces a cavity enhanced Raman spectrum (CERS).[27] Accurate values for the droplet's size and refractive index are retrieved from the wavelengths of the resonant Raman modes—commonly called Whispering Gallery Modes (WGMs) or morphology dependent resonances—in the droplet.[21,24,32] The WGMs arise as Raman scattered light is amplified in a spherically symmetrical droplet at discrete combinations of size, refractive index, and wavelength while the optical trap holds the droplet in air, acting as a low-loss resonating cavity. These two basic measurements of size and refractive index combined with the stable trapping of a particle enable direct real-time studies of aerosol physical properties with unprecedented precision and accuracy on levitated droplets surrounded by gas. Most studies thus far have focused on homogeneous single-phase droplets so that the existing data analysis algorithms developed by Preston and Reid can be employed.

However, there is evidence that a core–shell morphology is common in many aerosol systems,[7,19,24,27,33–40] demanding an effective way to accurately retrieve physical properties from spherically symmetrical core-shell droplets.[23,24,27,40] Core–shell morphologies dramatically change the particle's interfacial chemistry and properties, thus altering its interactions with radiation and reactive gases, its equilibration timescale with the gas-phase, and its ability to uptake water. Water uptake is a critical component of direct light scattering and also the activation of particles into cloud droplets and ice crystals.[41–44] Here we present an efficient computational approach for retrieving the properties of core–shell droplets that improves upon the methods we briefly described in Gorkowski et al.[24] and rigorously test the accuracy of this new algorithm.

WGMs are morphological resonances inside a spherical droplet that form a standing wave around the droplet's circumference. Since WGMs depend on the morphology of the droplet, they can be used to distinguish between a homogeneous droplet and a core–shell droplet. Further, the lack of WGMs can indicate a non-spherical partially-engulfed morphology.[15,16,19,27,39] However, studies of core–shell droplets have to-date been limited to select cases with additional constraining information. A previous algorithm required *a priori* WGM labels specifying the mode number, mode order, and electromagnetic wave type (either transverse electric (TE) or transverse magnetic (TM)) for each WGM.[45] Another way to constrain the fit is to assign the refractive index (m) and chromatic dispersion ($\mathrm{d}m/\mathrm{d}\lambda$) of the core and shell *a priori*, and then fit the diameter of the core and shell, and the WGM labels.[23,39] Clearly *a priori* knowledge of the droplet's properties is not possible in many aerosol systems, especially realistic complex chemical systems. Lastly, in our previous work we implemented an exhaustive direct search approach that could fit an isolated set of WGMs with no additional constraints but which took 24 to 48 hours for each Raman spectral frame measured every 2 seconds.[27] This approach is too computationally expensive to analyze AOT experimental datasets that are often acquired over many hours. Here we present an improvement of our earlier algorithm that can now fit an individual set of WGMs in one Raman frame in less than 10 minutes using a personal computer. However, a typical AOT experiment lasting 6 hours generates 11,000

individual spectra, and so treating the entire experiment as a set of independent spectra would still require approximately of 51 days to analyze. Since the spectra are not independent, we use comprehensive fits of the WGMs in a small subset of the spectra to then assign the WGM labels for the rest of the spectra collected, reducing the total computation time to a day or less.

2. Experimental

2.1 Whispering Gallery Mode Theory

The solutions for Mie light scattering from homogeneous droplets and core–shell droplets have been studied and used extensively.[21,32,45–52] Using Lorenz-Mie scattering theory, we numerically solve for the whispering gallery modes, which are sharp resonances in the broader Mie scattering band. We follow the solution form presented in Bohren and Huffman,[53] and shown in the Supplemental Information. The WGM resonances correspond to standing electromagnetic waves with an integral number of wavelengths that form around the circumference of a spherically symmetrical droplet. When the spherical symmetry is broken, the standing waves do not exist.

The WGM resonances occur when the denominator of the Mie scattering coefficient vanishes. Therefore, to find the resonance position, we set the denominator equal to zero and solve for the Mie size parameter (χ) given a refractive index (m), mode number (n), and mode order (o). The Mie size parameter is a dimensionless number relating the circumference of the particle (πd_p) to the wavelength (λ) of the light: $\chi = \pi d_p / \lambda$. The homogeneous case has an approximate analytical solution; however, we use this only as a starting point for the numerical solution, as Preston and Reid[21] demonstrated that this analytical approximation has significant errors in the resulting resonance position. However, it is sufficient to constrain the mode order, which usually has a small integer range of o = 1, 2, or 3 (higher mode orders are typically too faint to measure). Given the mode order, we then solve Eqn. (1) for the transverse magnetic and Eqn. (2) for the transverse electric resonances for a homogeneous sphere. The solution utilizes Riccati-

Bessel functions ξ_n, ψ_n, and χ_n , with a prime indicating the first derivative with respect to the argument.

$$0 = m\psi_n(m\chi)\,\xi_n'(\chi) - \xi_n(\chi)\,\psi_n'(m\chi) \tag{1}$$

$$0 = \psi_n(m\chi)\,\xi_n'(\chi) - m\xi_n(\chi)\,\psi_n'(m\chi) \tag{2}$$

For a core–shell system, the standing wave propagates in two distinct dielectric materials, and the solution is very sensitive to both materials when the thickness of the shell is comparable to the wavelength of the resonating light. For the core–shell solution, we again set the scattering coefficient's denominator equal to zero. We then derive Eqn. (3) for the transverse magnetic resonance and Eqn. (4) for the transverse electric resonance. In the core–shell notation, we added subscripts for the shell (s) and core (c) refractive index, the core radial fraction (f_c), and the Mie size parameter (χ) is defined by the shell diameter. The influence of the core is folded into two additional terms A_n and B_n which are defined in Eqns. (5) and (6).

$$0 = \xi_n(\chi)[\,\psi_n'(m_s\chi) - A_n\,\chi_n'(m_s\chi)] - m_s\xi_n'(\chi)[\,\psi_n(m_s\chi) - A_n\,\chi_n(m_s\chi)] \tag{3}$$

$$0 = m_s\xi_n(\chi)[\,\psi_n'(m_s\chi) - B_n\,\chi_n'(m_s\chi)] - \xi_n'(\chi)[\,\psi_n(m_s\chi) - B_n\,\chi_n(m_s\chi)] \tag{4}$$

$$A_n = \frac{m_s\psi_n(m_s\chi f_c)\psi_n'(m_c\chi f_c) - m_c\psi_n'(m_s\chi f_c)\psi_n(m_c\chi f_c)}{m_s\chi_n(m_s\chi f_c)\psi_n'(m_c\chi f_c) - m_c\chi_n'(m_s\chi f_c)\psi_n(m_c\chi f_c)} \tag{5}$$

$$B_n = \frac{m_s\psi_n(m_c\chi f_c)\psi_n'(m_s\chi f_c) - m_c\psi_n(m_s\chi f_c)\psi_n'(m_c\chi f_c)}{m_s\chi_n'(m_s\chi f_c)\psi_n(m_c\chi f_c) - m_c\psi_n'(m_c\chi f_c)\chi_n(m_s\chi f_c)} \tag{6}$$

To initialize the numerical solution for the core–shell WGMs, we start with a core fraction of one and use the homogeneous solution. Then we incrementally decrease the core fraction in variable step sizes of 10^{-4} to 10^{-8}. We decrease the step size when the numerical solution results in a non-smooth change from the previous result.

Using the numerical solutions to Eqns. (1-6) we generate a database of Mie resonances for both droplet morphologies. The homogeneous database returns a Mie resonance given a refractive index (m) and WGM label (l), which corresponds to a specific transverse electric or transverse magnetic resonance, mode number, and mode order. The

mode number corresponds to the number of standing wave nodes that are along the interior surface of the droplet. The mode order corresponds to the number of standing wave nodes in the radial direction from the surface of the droplet – these are essentially higher order resonances. Either the electric or the magnetic field can be transverse, indicating which field of the electromagnetic wave is propagating parallel to the droplet's surface. The core-shell database returns a Mie resonance given a shell-refractive index (m_s), core-refractive index (m_c), core-fraction (f_c) and WGM label. The core-fraction denotes where along the droplet's radial axis the refractive index changes between the core and the shell phases. Refractive indexes change as a function of wavelength, therefore to constrain the refractive index dependence on wavelength we use a chromatic dispersion relation, Eqn. (7) following Preston and Reid,[21] where m_0 is the refractive index at a specified wavelength (typically 650 nm for a 532 nm trapping laser) and m_1 is the dispersion term which accounts for the wavelength dependence. This refractive index dependence on wavelength is also used in the inverse fitting to constrain the fit as the WGM positions are measured across a range of wavelengths.

$$m_\lambda = m_0 + m_1\left(\frac{1}{\lambda} - \frac{1}{\lambda_0}\right) \quad (7)$$

Using the database for the homogeneous case, we can generate WGM values simulating different experimental conditions. Shown in Figure 1 is a simulation of single-phase particle growth at a constant refractive index. As the droplet grows, the WGM resonant frequencies increase in Raman-shift wavelength uniformly; the curves showing the resonances are parallel in the Figure. Nearly overlapping WGMs will result in merged peaks in the measured data, but this is not detrimental to the fitting. While for any given pair of indices the WGMs progress in sequence (i.e., TM^1_{62}, TM^1_{63} TM^1_{64},...), the overall sequence of all of the WGM labels at a given diameter is not universal because the relative positions depend on refractive index. We show a similar plot to Figure 1 in the Supplemental Information for refractive index and chromatic dispersion dependencies. For a homogeneous droplet, the diameter is the most sensitive parameter to WGM position, with a change of 0.66 nm in the retrieved d_p per 1 cm^{-1} change in the WGM's

Raman shift. The refractive index (9.5×10^{-5} (m_0)/cm^{-1}) and a chromatic dispersion (0.004 μm (m_1)/cm^{-1}) are less sensitive. These sensitivities are the average slopes of the WGMs across droplets of typical size and composition; see the Supplemental Information for more details.

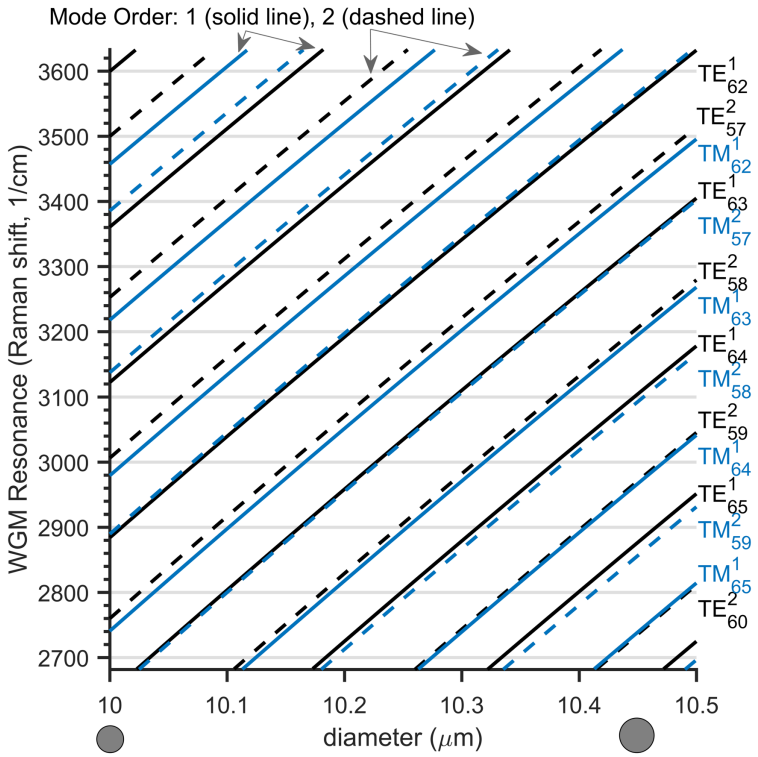

Figure 1. Calculated whispering gallery mode (WGM) positions as a homogeneous 10 μm droplet grows by 500 nm in diameter, at a constant refractive index of 1.37. The WGM resonance wavelength is converted to a Raman shift from 532 nm incident light, consistent with standard AOT experiments. Select WGM labels are indicated by TE for transverse electric (black) and TM for transverse magnetic (blue). The superscript is the mode order and the subscript is the mode number. Solid lines are mode order 1 and dashed lines are mode order 2.

The parallel nature of the homogeneous WGM solutions shown in Figure 1 does not translate to the core–shell WGMs. We generated core–shell WGM values simulating the addition of a shell phase onto a core phase, shown in Figure 2. The WGM series do not evolve in parallel because the different mode orders of the standing wave have a different radial penetration depth and thus a different relative sensitivity to the dielectric properties of the shell and the core. This broken symmetry is a strong identifying characteristic of core-shell droplets. Mode order 1 is more sensitive to changes at the droplet's outer surface where the shell resides than mode order 2 is, as this mode order traverses more deeply into the droplet. The transverse electric WGMs have a sharper radial intensity distribution than the transverse magnetic modes, which also contributes to the non-parallel evolution. From Figure 2 we also observe that WGMs that were overlapping in the homogeneous spectrum become resolvable because they split in their Raman shift positions when the shell grows. This WGM peak splitting and non-parallel

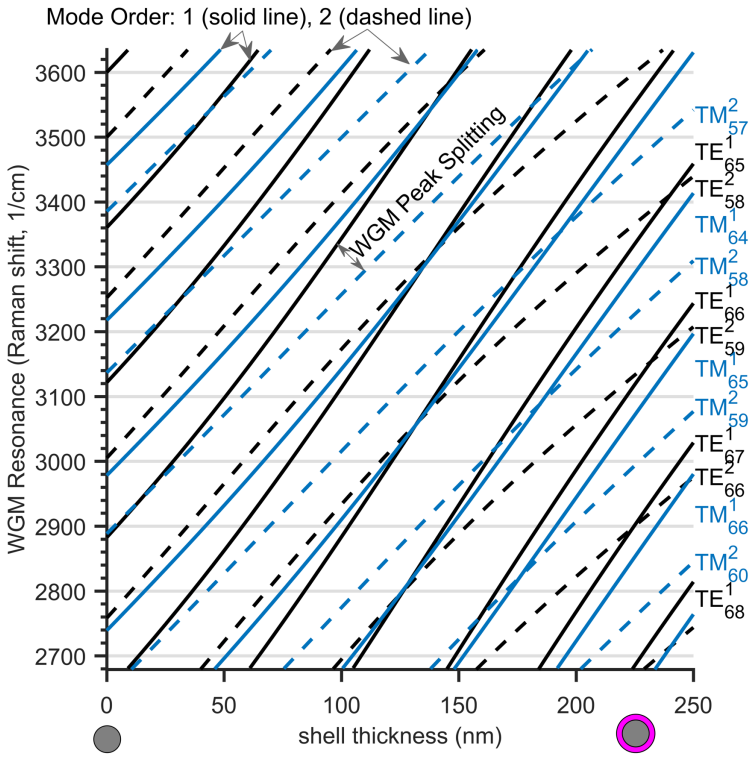

Figure 2. Calculated WGM positions for a core–shell droplet with a constant 10 µm diameter core with a constant refractive index of 1.37, as in Fig. 1. Growth adds a shell with refractive index 1.45 and the thickness indicated on the x-axis. The WGM labels follow the same notation as Fig. 1.

WGM evolution with changing size are qualitative patterns that can be used to distinguish core–shell WGMs from homogenous WGMs. More broadly, the non-parallel evolution indicates a radial gradient in properties near the droplet surface with a length scale of 10s to 100s of nm, smaller than the wavelength of the trapping laser.

2.2 Inverse Algorithms for WGM Analysis: Overview

We developed an inverse optimization algorithm that applies to both the homogeneous and the core-shell morphology. The goal of the algorithm is to efficiently and accurately match the WGM positions identified in the Raman spectrum to a specific combination of diameter and refractive index using Mie theory. In this inverse problem we are optimizing the diameter (d_p), the refractive index (m_0) along with dispersion (m_1) as described in Eqn. 7, and the specific WGM labels (l) as displayed in Figures 1 and 2. We first describe existing algorithms and how the problem scales geometrically as the number of parameters increases. We then preceded to outlining the optimization of a single spectral frame of data, starting with how to internalize optimization of d_p and therefore decrease the parameters directly searched for by one. We then discuss how the combinations of discrete WGM labels are found. Lastly, we present the procedure for optimization of the refractive index parameters (m_0, and m_1). We then take another step back and discuss how we can use a full time series of WGMs to further constrain each WGM label (l). As finding the optimum set of WGM labels constitutes a large fraction of the computational time, avoiding this attribution for most data frames makes the analysis significantly more efficient.

2.3 Algorithm Optimization

Existing algorithms for WGM analysis of homogeneous droplets are a combination of direct search and least-squares minimization.[21,23,32,54] In a direct search the computation scales as the number of parameters (d_p, m_0, m_1, and l); for a homogeneous droplet that is n^4 for a single spectral frame (n_{frame}). An improvement to this was first proposed by Preston and Reid[32]. Their algorithm uses a low-resolution search and subsequent refinement using an R-squared minimization. This results in a scaling of approximately $(n^3+1)n_{frame}$, resulting in a one-second fit time per frame. To extend to a

core–shell parameter space using a fully direct search across all the fit parameters would result in a $(n^7)n_{frame}$ scaling (d_p, f_c, m_{C0}, m_{C1}, m_{S0}, m_{S1}, and l). Our initial implementation of this direct search resulted in a fit time of 24 to 48 hours per frame using a personal computer depending on step size and parameter ranges, making this approach unrealistic even if performed on a cluster. This geometric scaling of the direct search algorithm makes the core–shell implementation unfeasible to analyze experimental data sets routinely, as n_{frame} can typically exceed 10,000.

Our algorithm overcomes this computational challenge through three innovations. First, we internalize the d_p search via the Mie size parameter ($\chi = \pi d_p/\lambda$) so that it is now an internal constraint, thus decreasing the scaling by one factor. Second, we employ a random search (n_{rand}) over f_c, m_{C0}, m_{C1}, m_{S0}, and m_{S1} to find possible sets of WGM labels (n_{pWGM}). Third, we take the individual WGMs and group them temporally into WGM sequences (n_{seq}), such that each sequence has a single WGM label (see the Supplemental Information for an example). This results in an approximate single-frame scaling for a homogeneous droplet of $(n_{\text{rand}}n_{\text{seq}}+n^2)n_{\text{pWGM}}$ and for a core–shell droplet of $(n_{\text{rand}}n_{\text{seq}}+n^5)n_{\text{pWGM}}$. Once the labels are known for each of the n_{groups} then the scaling for the time series is n^2n_{frame} for homogeneous droplets and n^5n_{frame} for core–shell droplets. The resulting fit time for the homogeneous case is 2.6 seconds per frame for unlabeled WGMs and 9 ms per frame for labeled WGMs. For the core–shell case, it is 6.8 minutes per frame for unlabeled WGMs and 0.57 seconds per frame for labeled WGMs. We provide an outline of the complete algorithm in the Supplemental Information.

2.4 Fitting a Single Raman Spectrum

Our first efficiency gain was to convert d_p into an internal constraint. This uses the Mie size parameter (χ) to relate the given WGM positions to each other. As d_p can be assumed to be constant in a single spectral frame the positions of the first WGM (λ_1) can be related to another WGM (λ_i) as shown in Eqn. (8), where χ_i is the Mie resonance for the i^{th} WGM, and χ_1 is a possible Mie resonance for the first WGM.

$$\chi_i = \frac{\lambda_1}{\lambda_i}\chi_1 \tag{8}$$

The possible values for χ_1 are determined by the search space of WGM labels (l); in this way, we constrain the range of possible d_p. This approach is very sensitive to the accuracy of the initial λ_1, which can be the location of any of the observed WGMs. Consequently, we initialize the search with several λ_i values, up to the full set of observed WGMs. In practice, a comprehensive search showed no systematic improvements over using only the first WGM, but to be cautious we initialize the search with the three largest amplitude WGMs. This method of relating one Mie resonance to another internalizes the diameter constraint so that we only need to search across the possible WGM label combinations.

The number of possible WGM labels combinations does not need to be exhaustive as we only need to track the best possible combinations. Consequently, we initiate the search with random values for m_0 and m_1 for a homogeneous droplet, or for m_{S0}, m_{S1}, m_{C0}, m_{C1} for core–shell droplets, and using a direct search for f_c. Then for each random guess we start with all possible WGM labels for the first WGM, l_1, and then sequentially find the best label for the next WGM in the measured spectrum. The minimization for the next l_i follows by calculating the squared error for each possible l by setting Eqn. (8) equal to zero and squaring the result to get Eqn. (9). To account for neighboring WGM peaks, we keep the 3-5 closest WGM labels that minimize the squared error. We then repeat this process for the next WGM, etc. After a set number (i) of such WGM searches we remove a fraction (0.5 to 0.8) of the poorest WGM label sets to reduce the computational load; however, we keep a minimum of 100 WGM label sets. Consequently, the WGM sets that result in a high error are rapidly removed and are not propagated through the rest of the computation. This process results in the 100 best possible WGM-label sets for a given random guess. The random guess is then repeated until the probability of finding a new and unique WGM-label set is less than 0.25%. For a homogeneous system, we average 213 unique WGM-label sets and for a core–shell system we average 488 unique WGM-label sets.

We then globally optimize each of the possible WGM label sets across their droplet properties: m_0 and m_1 for a homogeneous droplet and m_{S0}, m_{S1}, m_{C0}, m_{C1}, and f_c. for a core-

shell droplet. The global optimization proceeds in two steps. The first is a gridded minimization finding the minimum based on the squared error of the Mie-size parameter:

$$squared\ error = \sum_{i=2}^{WGM\ count} \left(\frac{\lambda_1}{\lambda_i}\chi_1 - \chi_i\right)^2 \quad (9)$$

We use a gridded search because the error landscape is non-smooth and non-convex with multiple local minima. We tested multiple gradient descent and global search algorithms, but to achieve reliable results they required more computational time than the simpler gridded search algorithm. We achieved an efficient gridded search for the many WGM-label combinations and higher dimensional parameter space in the core–shell fit using GPU computations instead of CPU computations as we found that a 4-core CPU desktop with a GPU was 39% faster than a cluster of 32 CPUs.

After we complete an initial global search we carry out a local refinement of the putative optimal solution using a gradient decent algorithm optimizing the reduced chi-squared value (χ^2_{red}) of the retrieved diameters (d_i) calculated from the Mie size parameter, shown in Eqn. (10). We find the optimal diameter ($\overline{d_p}$) by taking the average of each d_i calculated from each Mie size parameter. We propagate the measurement error (σ_i) from the Gaussian fit of the WGM resonance peak in the spectrum.

$$\chi^2_{red.} = \frac{1}{WGM\ count - variable\ count} \sum_{i=1}^{WGM\ count} \left(\frac{d_i - \overline{d_p}}{\frac{\chi_i \sigma_i}{2\pi}}\right)^2 \quad (10)$$

The optimum WGM-label set can now be found by ranking the retrieved χ^2_{red} for each WGM-label set. From simulation results shown in Figure 3 the optimum WGM-label set is not always the correct one. Near the optimum each of the WGM-label sets tends to only have one or two WGMs of differing labels, leading to a multiple minimum with similar physical properties. To account for that we use multiple Raman spectral frames containing the same WGM sequences, which is described below, or we take an average result of the multiple minima. This averaged result is the mean of all WGM-label sets that have a χ^2_{red} error that is lower than the lowest χ^2_{red} error plus a 1σ critical value. This 1σ

critical value is based on the degrees of freedom and the cumulative probability of a chi-squared distribution. For a homogeneous optimization, this 1σ critical value is 3.5 and for a core–shell optimization it is 7.0. We call this type of fitting the 1σ WGM labeled fit. This final averaging step in the 1σ WGM labeled fit increases the error in the fit but tends to gain a more self-consistent result because it averages the degenerate solutions caused by overlapping WGM labels.

2.5 Fitting a Full Raman Spectral Time Series

The last improvement to the optimization algorithm is to sort the individual WGMs into sequences. This process starts with the first frame of WGMs and places neighboring WGMs in the next frame into sequences based on the previous frame. If there is no sequence within the variable threshold (typically 0.2 nm), then that individual WGM creates a new sequence. This process is then repeated for the full experiment resulting in 100s to 1000s of WGM sequences; an example is shown in the Supplemental Information. The labeling of the WGM sequences follows the same random search process as described above, but in this case we average the χ^2_{red} value across multiple Raman spectra that contain the same set of WGM sequences, and therefore the same WGM-label sets. This averaging of χ^2_{red} helps resolve which WGM within the 1σ WGM labeled fit has a consistently low error across multiple frames and is thus more likely the correct label. For this averaging to be effective we typically use 10 frames for a homogeneous system and 50 frames for a core–shell system. Even with this averaging of multiple frames there are sometimes still multiple WGM-label sets within the 1σ critical value – this is where our algorithm can misidentify a WGM label due to it being too close to another WGM. Further work in incorporating additional information into the algorithm is being pursed, such as using the peak amplitude to constrain the possible WGM labels (TM peaks tend to be smaller than TE peaks) and using the initial fit to find additional WGMs of lower amplitude in the Raman spectrum.

Once the WGM series all have a WGM label, then we fit the full time series using the previously discussed global optimization of m_0, m_1, and d_p for a homogeneous droplet and of m_{S0}, m_{S1}, m_{C0}, m_{C1}, d_p and f_c for a core–shell droplet. Since fitting a set of core–shell

WGMs is much faster if the WGM labels are known, fitting the full time series can be achieved when the WGMs are grouped into sequences. Using the WGM sequences results there are fewer unlabeled fits that need to be completed.

3. Results and Discussion

3.1 Assessment of Algorithm's Performance

To assess our new inverse fitting algorithm, we generated WGM positions for a simulated droplet and then added random Gaussian noise to the individual WGM positions. Our random noise used a sigma of 0.01 nm, shown by Preston and Reid[21] to be typical for measured WGMs and consistent with the uncertainty of the Raman spectrograph used (Princeton Acton). We simulated all possible WGM labels up to mode order 2 between 620 nm and 660 nm, which is representative of our typical Raman spectrum acquisition using a 532 nm trapping laser and a 1200 grooves/mm diffraction grating.[24,27] After finding all possible WGMs, we randomly selected a subset to use in the fit. We progressively added WGMs to the initial random set to probe how the uncertainty changes with the number of WGMs used in the fit. We then repeated this process 300 times by generating a new set of droplet properties randomly, based off of our typical range of observed parameters (these are listed in the Supplemental Infromation). This means that each simulation is a new droplet with a diameter between 9 μm to 11 μm and a refractive index between 1.37 to 1.42. For this assessment, we used the algorithm to fit a single Raman spectrum (frame) and did not incorporate any time evolution in the fit. We describe the details of the simulation bounds as well as a comparison of computation times in the Supplemental Information.

Using the simulation results we determined whether the calculated (presumably global) minimum fit gave the known correct WGM-label set. We also determined whether the correct WGM label set was within the 1σ critical value of the global χ^2_{red} minimum (defined above) regardless of whether it was the optimal fit. We show these two cases in Figure 3 for both a homogeneous and a core–shell droplet. The solid curves in Figure 3 indicate that the correct WGM label is not always at the minimum, but that the probability rises with the number of WGMs used in the fit. This result is less of a concern for a homogeneous droplet as there are usually more than 4 WGMs in a typical spectrum, where the attribution accuracy is over 95%. However, for the core–shell droplet the additional fit parameters increase the degeneracy in fitting incorrect WGM labels and the attribution accuracy remains below 90% for even 12 WGMs. The increased probability for the minimum of a core–shell droplet to be incorrectly labeled is why we implemented

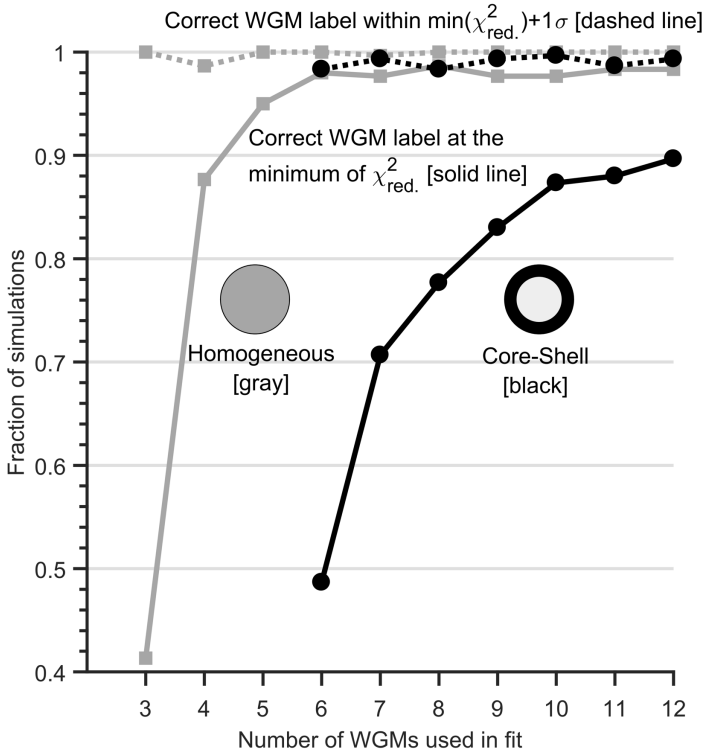

Figure 3. WGM labeling results for simulated droplets with a homogeneous (gray) or core–shell (black) morphology. The fraction of simulated fits that had the correct WGM label set at the minimum χ^2_{red} error is shown with a solid line. The fraction of simulated fits that had the correct WGM label set within the minimum χ^2_{red} error plus 1σ is shown with a dashed line.

358 the 1σ critical range of the global χ^2_{red} minimum. Figure 3 also shows that the correct
359 WGM-label set is near the minimum even if it is not at the minimum due to noise added
360 and the inherent flexibility in the model. That is one reason why we implemented WGM
361 grouping as it helps resolve which WGM label is consistently the minimum across
362 multiple measured spectra.

363 Using the simulated WGMs and their resulting fits we assessed the error in the
364 resulting droplet parameters retrieved by the algorithm: diameter (d_p) and refractive
365 index (m). We examined two cases: (1) with the correct WGM label assignments what is
366 the global minimum (solid lines); and (2) for all fit results that are within the 1σ critical
367 range of the global χ^2_{red} minimum (dashed lines), what is the average error. The first case
368 applies if, by using multiple measured spectra (frames), we can determine which WGM
369 label set is the most consistent, and therefore correct. The second case quantifies the
370 variability in the 1σ range of the global χ^2_{red} minimum. We report the error of the fitting
371 as the standard deviation of the difference between the simulated parameter and the
372 resulting fitted parameter. In Figure 4 we show the error in droplet diameter as a function
373 of WGMs used. The error in the homogeneous droplet is consistent with the algorithm
374 developed by Preston and Reid[21], which achieved ±2.2 nm when fitting 12 WGMs. We
375 now provide an error assessment of the core and shell diameters. Our error in the shell
376 diameter (the total droplet diameter) is similar in magnitude to the homogeneous case,
377 but the error in the core diameter (total diameter – shell thickness) is significantly higher.
378 We attribute the increased error to the additional flexibility in the core–shell model. For

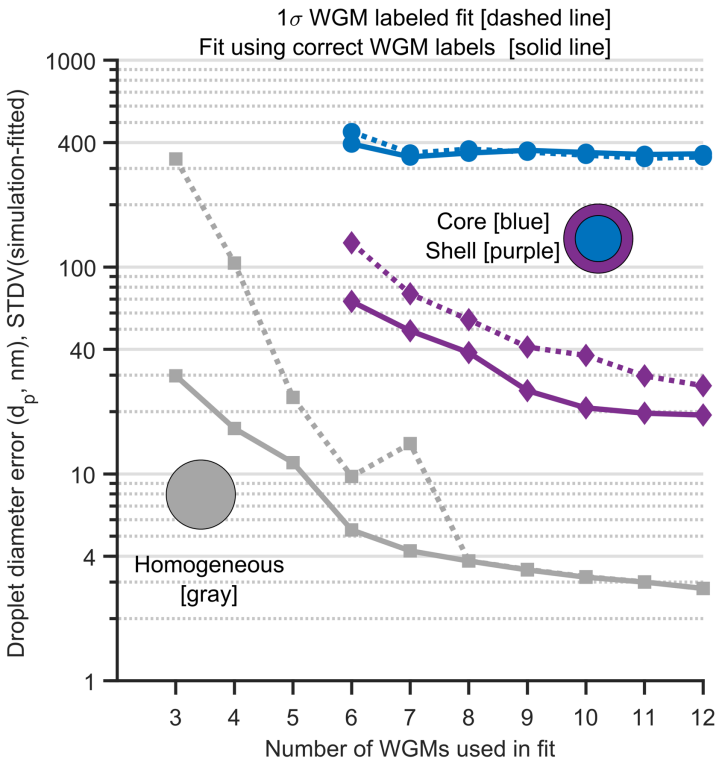

Figure 4. The fit error of a droplet's retrieved diameter (d_p) in a homogeneous or core–shell droplet versus the number of WGMs used in the fit. The error is the standard deviation of 300 simulated droplets with a d_p between 9 μm to 11 μm at each set of WGMs used. The solid line is the minimum using the correct WGM labels. The dashed line represents the mean radius of the multiple minimums in the fits with a cut-off value of being everything within 1σ of the global minimum.

experimental systems we try to fit data with at least 2 more WGMs than the minimum required. For a homogeneous droplet this means 5 or more WGMs, and for core–shell droplet this means 8 or more WGMs. Using that minimum threshold, we then averaged across the remaining fits to get a typical error for any one experiment, this is tabulated in the Supplemental Information. The fractional (percent) error of the various parameters puts them into context; for a homogeneous particle, the fractional error in d_p is 0.045% and for a core-shell particle, the fractional error in d_{shell} is 0.024% and the fractional error in d_{core} is 3.8%. When we fit experimental data we know the initial diameter of the homogeneous droplet and this helps to constrain the possible diameters of the core-shell fit once the outer shell phase has formed or been added.

We evaluated the error in retrieving the refractive index using the same procedure. Our refractive index dispersion model has two fit parameters to account for the small change in refractive index as a function of wavelength. In Figure 5 we plot the error in the first parameter, m_0, which for our simulation is equivalent to the refractive index at 650 nm, $m_{650\,nm}$. We typically use $m_{650\,nm}$ as that corresponds to our WGM observations of the broad O–H Raman mode with a Raman shift value of ~3400 cm^{-1}. The dispersion term (m_1) plays a necessary, yet minor role compared to m_0 and d_p. We provide a plot of the error in the dispersion term in the Supplemental Information. The error in the refractive index for the homogeneous droplet is consistent with Preston and Reid,[21] which achieved ±0.00033 with 12 WGMs. In the case of the core–shell droplet, after nine WGMs the level of improvement in the fit with each additional WGM diminishes. We interpret this as a

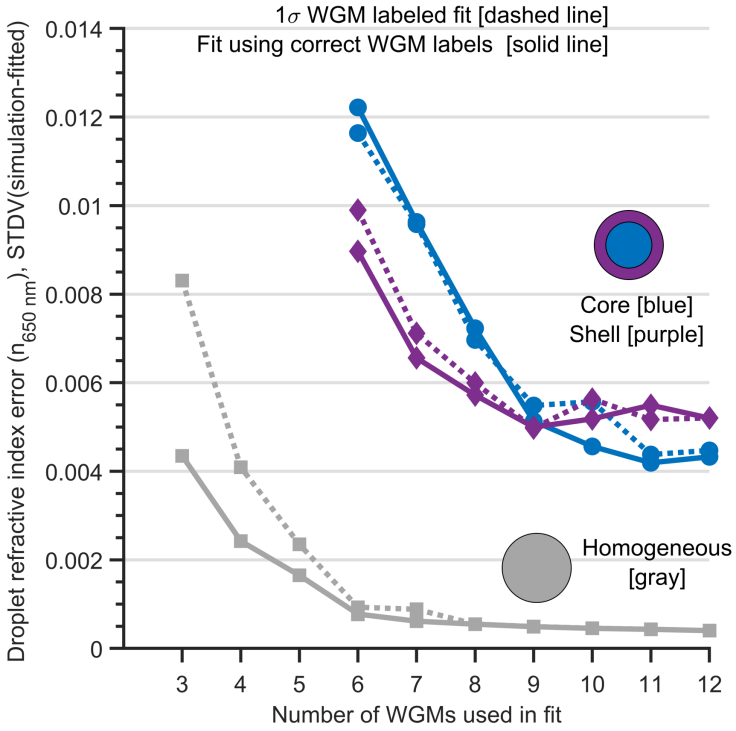

Figure 5. The refractive index (m_0) fit error of a homogeneous and core–shell droplet's WGMs versus the number of WGMs used. The error is the standard deviation (STDV) of 300 simulated droplets with a m_0 between 1.37 to 1.42 (homogeneous) at each set of WGMs used. The core–shell droplet had a m_{C0} between 1.37 to 1.42 and m_{S0} of 1.40 to 1.45. The solid line is the minimum using the correct WGM labels. The dashed line represents the mean radius of the multiple minimums in the fits with a cut off value of being everything within 1σ of the global minimum.

minimum error asymptotic limit determined by the simulated noise added to the WGM positions. Some future improvements could incorporate the amplitude of the WGM as well as the width of the WGM as additional information, which may further improve the fit accuracy.

So far we have focused on simulations of data from the O–H Raman scattering band. In some cases (i.e. a hydrophilic hydrocarbon shell) only the C-H Raman band shows significant features. There are limitations to the fitting of WGMs when only the C–H Raman scattering band common to organic carbon phases is measured (much narrower than the broad O–H Raman mode for H_2O), leading to fewer WGMs available for the fitting.[24,27] To still gain some insight into the pure organic carbon systems we use *a priori* information on the refractive index of the core phase to reduce the size of the feasible parameter space, but even then the fits are not as well constrained as fits for systems with the much broader O–H Raman signal present in aqueous phases.

3.2 Spectral Response from Adding a Shell of Organic Carbon to an Aqueous Inorganic Droplet

We use the addition of α-pinene secondary organic aerosol (SOA) (formed by gas-phase ozonolysis of α-pinene vapor) to an NaCl(aq) droplet to explore how the droplet's Raman spectrum and WGMs transition from a homogeneous droplet to a core-shell droplet when a second phase (the SOA) is added.[24] This experiment, shown in Figure 6, clearly demonstrates how the homogeneous fit becomes unrealistic for a core–shell droplet after just a thin shell forms on the droplet. Figure 6 also shows the WGM peak splitting caused by the growth of a shell on a previously homogeneous core as predicted from the theoretical results shown in Figure 2. The experiment began with a trapped NaCl(aq) droplet at roughly 75% RH. We then flowed ozone (3.4 ppm) and α-pinene vapor (182 ppm) into the chamber, forming SOA at t=0 minutes. The experimental methods are described in the Supplemental Information, and in Gorkowski et al.[24] The majority of the SOA shell growth was caused by coagulation of submicron SOA particles onto the trapped NaCl(aq) droplet. A detailed assessment of this aerosol system was

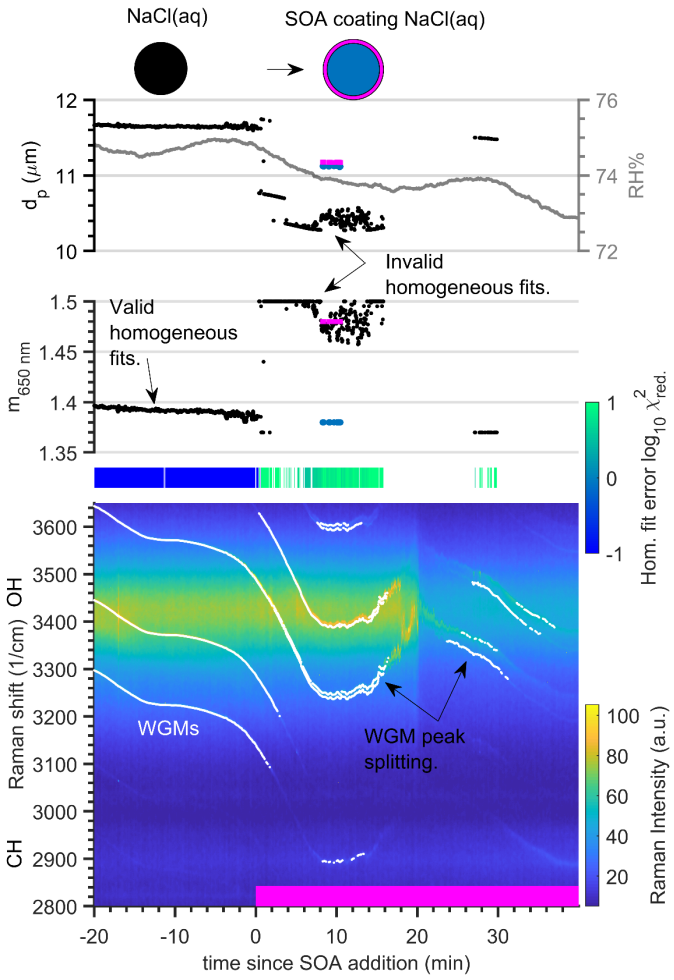

Figure 6. Raman spectral time series for a tweezed aqueous NaCl droplet with the addition of an α-pinene SOA coating. Raman spectra are shown in the bottom graph, and the white points indicate the positions of detectable whispering gallery modes (WGMs). The decreasing slope of the WGM traces indicates the droplet is evaporating due to the RH decrease. The α-pinene SOA flow reaction started at 0 min, indicated by the pink bar. The droplet's effective refractive index ($m_{650\,nm}$) and diameter (d_p) retrieved every two seconds from the WGM analysis are shown in the middle and top panels. The RH is shown in the top right panel. The decrease in the diameter of the droplet following coating is due to a decrease in the RH of the chamber, causing evaporation of water. The fit results of the WGM positions to a homogeneous Mie model are in the top two panel as black dots. The fit error for the homogeneous model is shown in the green/blue bar, where consistently blue indicates a valid fit and green indicates an invalid fit to the model. The core–shell fitting is then used to retrieve the properties of the NaCl(aq) core (blue points) and α-pinene SOA shell (pink points) at 10 min.

previously discussed in Gorkowski et al.[24] We use the core–shell fit results as guides for this system due to the limited number of WGMs (6 per frame) and limited total number

of frames (24) available to constrain the core–shell model. The retrieved refractive indices are consistent with a NaCl(aq) core and SOA shell, when compared to our previous work.[24] The retrieved shell thickness was ~25 nm, which highlights the resolving power of the WGMs. In Figure 6 we should also note that the downward trend in WGM position is also consistent with the decrease in size observed in the core–shell fit as well as the decreasing RH. Lastly, the decreasing intensity of the WGMs after 15 minutes is attributed to a formation of an emulsion of SOA in the aqueous NaCl core as discussed in Gorkowski et al.[24]

3.3 Evaporation of an Organic Carbon Core through an Organic Shell

We investigated our ability to measure phase-separated particles and the resulting partitioning between the two phases using the coagulation of squalane ($C_{30}H_{62}$, a hydrophobic long-chain hydrocarbon) onto an aqueous glycerol droplet. We observed liquid–liquid phase-separation of these two compounds in beaker experiments, so we expect phase-separation in the AOT. However, the actual morphology of the phase-separated droplets remained unknown until our AOT experiments. The persistent WGMs confirm a core-shell morphology (as opposed to a partially engulfing lens), with glycerol forming the core.[27,39]

In Figure 7 we show the core–shell fit results for an isolated part of the experiment after we coagulated the squalane and coagulated additional glycerol to grow the droplet. We used coagulational growth so that the droplet was large enough to identify more than 6 WGMs per frame. The fits shown in Figure 7 are for the 270 minutes (6603 spectral frames) where the relative humidity (RH) was stable, and therefore composition was constant. Under these stable RH conditions the core of the droplet is predominantly glycerol, which continuously evaporates into the conditioned air due to its higher vapor pressure; to a lesser extent the squalane shell also evaporates. This evaporation is reflected in the fit as the diameter of the particle continuously decreases.

Our measurements are consistent with sparing but non-zero solubility of squalane and glycerol. The average shell refractive index, m_{650nm}, was 1.4359 ± 0.0042 which is

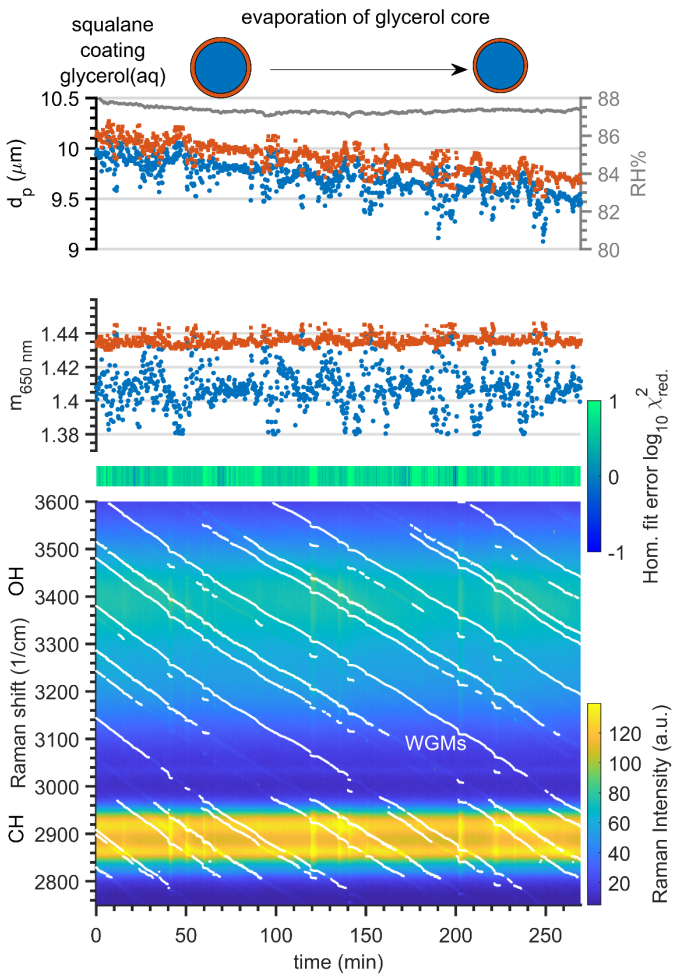

Figure 7. Raman spectral time series for a tweezed aqueous glycerol droplet coated with squalane. The evaporation of the glycerol core is observed from the decreasing trend in droplet diameter (d_p). The panels follow the same format as in Fig. 6. The retrieved two-second Raman spectral frames are averaged to 15 seconds for clarity.

458 lower than pure squalane ($m_{589\text{nm}} = 1.4474 \pm 0.0002$[55]). This indicates a measurable amount
459 of the aqueous glycerol absorbed in the squalane shell phase. Though our measured
460 refractive index is at a different wavelength than the reference value, these should still be
461 comparable given that the difference in wavelengths is small and as such the dispersion
462 would only decrease the refractive index by ~0.001 between 589 nm to 650 nm. The core
463 is also not a just a glycerol and water solution as glycerol(aq). At 87.3% RH the pure
464 solution has mass fractions of 0.6 for w_{water} and 0.4 for $w_{glycerol}$ resulting in an effective
465 $m_{589\text{ nm}} = 1.384 \pm 0.008$.[56] In contrast we observed a core with a higher effective refractive

index with at $m_{650\ nm}$ = 1.4076 ± 0.0128 that must be due to mixing with squalane, which would increase the effective refractive index. The higher uncertainty in *m* relative to the simulated assessment (Fig. 7) is likely due to the simulation not matching the uncertainty of determining the peak positions from the Raman spectrum.

We have used this same fitting algorithm in our previous work on the mixing of secondary organic aerosol phases with aqueous NaCl, aqueous glycerol and squalane [24]. This algorithm allowed us to identify the morphology of the biphasic droplet and determine the shell of SOA did not limit equilibration of the core. We are working towards using the retrieved refractive indexes from the core–shell fitting to measure the phase composition of both the core and the shell, to directly study phase partitioning and solubility. Incorporation of a chemical thermodynamic equilibration model along with a refractive index mixing model will extend this analysis to more components and complex biphasic systems. With a method to determine the concentration of reactants we can probe the feedback between chemical reaction rates, compositions, and morphology with the biphasic system properties. This algorithm could probe the mechanisms behind the salting out effect of polymers from an aqueous inorganic phase and the elucidate the mechanisms behind the Hofmeister series that is widely-known in biochemical systems for describing the salting-in/out of proteins.[4] Similarly, biphasic pH measurements could be performed with a sufficiently accurate refractive index model. [57] The combined AOT measurment system and new core-shell algorithm facilitates biphasic studies of compounds in supersaturated inorganic solutions, which are often difficult to access expermentally.[27] Understanding how biphasic systems evolve and their effects is an active research topic in environmental chemistry, biochemistry, and atmospheric chemistry.

4. Conclusions

We have developed a practical and efficient algorithm for fitting WGMs for a core–shell biphasic droplet. In the process, we have added to the understanding of how WGMs

494 change as a second shell phase forms around a previously homogeneous trapped droplet.
495 The major difference in WGMs in homogeneous and core–shell droplets is the peak
496 splitting of adjacent WGMs which was predicted in Figure 2 and then demonstrated
497 experimentally in Figure 6. We then tested our new fitting algorithm on simulated data
498 for a homogeneous droplet achieving accuracies of ±4.6 nm (0.045%) in particle diameter
499 (d_p) for a ~10 μm droplet and ±0.00067 (0.058%) in refractive index (m) for droplet with a
500 refractive index of ~1.395. The same algorithm applied to a simulated core–shell droplet
501 achieved accuracies of ±24 nm (0.24%) in shell d_p, ±359 nm (3.8%) in core d_p, and ±0.0055
502 (0.37%) in core and shell refractive indices. Using our new algorithm, we analyzed an
503 AOT experiment on a trapped core–shell droplet of squalane coating glycerol(aq). The
504 retrieved refractive indices of the core and shell phases were used to inform the chemical
505 composition of each phase. This improved efficient analysis method for core–shell
506 droplets opens the door to future experiments that study the physicochemical properties
507 and dynamics of biphasic droplets using aerosol optical tweezers, and the possibility for
508 analysis in real-time.

509 **Conflicts of Interest.** There are no conflicts to declare.

510 **Acknowledgements**. This research was supported by the National Science Foundation
511 (CHE-1554941). KG acknowledges support from the Bertucci Fellowship from the College
512 of Engineering at Carnegie Mellon University. Jonathan Reid and James Walker at the
513 University of Bristol provided valuable input regarding the evaluation of our new WGM
514 fitting algorithm.

References

1 M. Iqbal, Y. Tao, S. Xie, Y. Zhu, D. Chen, X. Wang, L. Huang, D. Peng, A. Sattar, M. A. B. Shabbir, H. I. Hussain, S. Ahmed and Z. Yuan, Aqueous two-phase system (ATPS): an overview and advances in its applications, *Biol. Proced. Online*, 2016, **18**, 1–18.

2 K. Mochizuki, T. Sumi and K. Koga, Liquid-liquid phase separation of N-isopropylpropionamide aqueous solutions above the lower critical solution temperature, *Sci. Rep.*, 2016, **6**, 1–10.

3 B. Monterroso, S. Zorrilla, M. Sobrinos-Sanguino, C. D. Keating and G. Rivas, Microenvironments created by liquid-liquid phase transition control the dynamic distribution of bacterial division FtsZ protein, *Sci. Rep.*, 2016, **6**, 1–13.

4 Y. Zhang and P. Cremer, Interactions between macromolecules and ions: the Hofmeister series, *Curr. Opin. Chem. Biol.*, 2006, **10**, 658–663.

5 B. Bagchi, Water Dynamics in the Hydration Layer around Proteins and Micelles, *Chem. Rev.*, 2005, **105**, 3197–3219.

6 J. Hirschfelder, D. Stevenson and H. Eyring, A Theory of Liquid Structure, *J. Chem. Phys.*, 1937, **5**, 896–912.

7 M. A. Freedman, Phase separation in organic aerosol, *Chem. Soc. Rev.*, 2017, **46**, 7694–7705.

8 W. M. Aumiller and C. D. Keating, Experimental models for dynamic compartmentalization of biomolecules in liquid organelles: Reversible formation and partitioning in aqueous biphasic systems, *Adv. Colloid Interface Sci.*, 2017, **239**, 75–87.

9 A. Abe, J. Genzer, W. H. De Jeu, S. Kobayashi, L. Leibler, T. E. Long, I. Manners, E. M. Terentjev, M. Vicent, B. Voit, G. Wegner and U. Wiesner, *Self Organized*

Nanostructures of Amphiphilic Block Copolymers II, Springer Berlin Heidelberg, Berlin, Heidelberg, 2011, vol. 242.

10 C. Cai, D. J. Stewart, J. P. Reid, Y. Zhang, P. Ohm, C. S. Dutcher and S. L. Clegg, Organic Component Vapor Pressures and Hygroscopicities of Aqueous Aerosol Measured by Optical Tweezers, *J. Phys. Chem. A*, 2015, **119**, 704–718.

11 A. E. Haddrell, R. E. H. Miles, B. R. Bzdek, J. P. Reid, R. J. Hopkins and J. S. Walker, Coalescence Sampling and Analysis of Aerosols using Aerosol Optical Tweezers, *Anal. Chem.*, 2017, **89**, 2345–2352.

12 J. F. Davies, A. E. Haddrell, A. M. J. Rickards and J. P. Reid, Simultaneous analysis of the equilibrium hygroscopicity and water transport kinetics of liquid aerosol., *Anal. Chem.*, 2013, **85**, 5819–26.

13 J. Buajarern, L. Mitchem and J. P. Reid, Characterizing the Formation of Organic Layers on the Surface of Inorganic/Aqueous Aerosols by Raman Spectroscopy, *J. Phys. Chem. A*, 2007, **111**, 11852–11859.

14 J. W. Lu, A. M. J. Rickards, J. S. Walker, K. J. Knox, R. E. H. Miles, J. P. Reid and R. Signorell, Timescales of water transport in viscous aerosol: measurements on sub-micron particles and dependence on conditioning history, *Phys. Chem. Chem. Phys.*, 2014, **16**, 9819–9830.

15 J. P. Reid, B. J. Dennis-Smither, N.-O. A. Kwamena, R. E. H. Miles, K. L. Hanford and C. J. Homer, The morphology of aerosol particles consisting of hydrophobic and hydrophilic phases: hydrocarbons, alcohols and fatty acids as the hydrophobic component., *Phys. Chem. Chem. Phys.*, 2011, **13**, 15559–15572.

16 B. J. Dennis-Smither, K. L. Hanford, N. A. Kwamena, R. E. H. Miles and J. P. Reid, Phase, morphology, and hygroscopicity of mixed oleic acid/sodium chloride/water aerosol particles before and after ozonolysis., *J. Phys. Chem. A*, 2012, **116**, 6159–68.

17 A. M. J. Rickards, R. E. H. Miles, J. F. Davies, F. H. Marshall and J. P. Reid, Measurements of the sensitivity of aerosol hygroscopicity and the κ parameter to the O/C ratio., *J. Phys. Chem. A*, 2013, **117**, 14120–31.

18 B. J. Dennis-Smither, F. H. Marshall, R. E. H. Miles, T. C. Preston and J. P. Reid, Volatility and Oxidative Ageing of Aqueous Maleic Acid Aerosol Droplets and the Dependence on Relative Humidity., *J. Phys. Chem. A*, , DOI:10.1021/jp504823j.

19 J. Buajarern, L. Mitchem and J. P. Reid, Characterizing Multiphase Organic/Inorganic/Aqueous Aerosol Droplets, *J. Phys. Chem. A*, 2007, **111**, 9054–9061.

20 C. Cai, D. J. Stewart, T. C. Preston, J. S. Walker, Y. H. Zhang and J. P. Reid, A new approach to determine vapour pressures and hygroscopicities of aqueous aerosols containing semi-volatile organic compounds., *Phys. Chem. Chem. Phys.*, 2014, **16**, 3162–72.

21 T. C. Preston and J. P. Reid, Accurate and efficient determination of the radius, refractive index, and dispersion of weakly absorbing spherical particle using whispering gallery modes, *J. Opt. Soc. Am. B-Optical Phys.*, 2013, **30**, 2113–2122.

22 R. Power, J. P. Reid, S. Anand, D. McGloin, a Almohammedi, a Almohamedi, N. S. Mistry and a J. Hudson, Observation of the binary coalescence and equilibration of micrometer-sized droplets of aqueous aerosol in a single-beam gradient-force optical trap., *J. Phys. Chem. A*, 2012, **116**, 8873–84.

23 A. Moridnejad, T. C. Preston and U. K. Krieger, Tracking Water Sorption in Glassy Aerosol Particles using Morphology-Dependent Resonances, *J. Phys. Chem. A*, 2017, **121**, 8176–8184.

24 K. Gorkowski, N. M. Donahue and R. C. Sullivan, Emulsified and Liquid–Liquid Phase-Separated States of α-Pinene Secondary Organic Aerosol Determined Using Aerosol Optical Tweezers, *Environ. Sci. Technol.*, 2017, **51**, 12154–12163.

25 G. Hargreaves, N.-O. a Kwamena, Y. H. Zhang, J. R. Butler, S. Rushworth, S. L. Clegg and J. P. Reid, Measurements of the equilibrium size of supersaturated aqueous sodium chloride droplets at low relative humidity using aerosol optical tweezers and an electrodynamic balance., *J. Phys. Chem. A*, 2010, **114**, 1806–15.

26 B. R. Bzdek, L. Collard, J. E. Sprittles, A. J. Hudson and J. P. Reid, Dynamic measurements and simulations of airborne picolitre-droplet coalescence in holographic optical tweezers, *J. Chem. Phys.*, 2016, **145**, 054502.

27 K. Gorkowski, H. Beydoun, M. Aboff, J. S. Walker, J. P. Reid and R. C. Sullivan, Advanced aerosol optical tweezers chamber design to facilitate phase-separation and equilibration timescale experiments on complex droplets, *Aerosol Sci. Technol.*, 2016, **50**, 1327–1341.

28 R. M. Power and J. P. Reid, Probing the micro-rheological properties of aerosol particles using optical tweezers, *Reports Prog. Phys.*, 2014, **77**, 074601.

29 R. E. H. Miles, J. S. Walker, D. R. Burnham and J. P. Reid, Retrieval of the complex refractive index of aerosol droplets from optical tweezers measurements, *Phys. Chem. Chem. Phys.*, 2012, **14**, 3037.

30 J. S. Walker, J. B. Wills, J. P. Reid, L. Wang, D. O. Topping, J. R. Butler and Y.-H. Zhang, Direct comparison of the hygroscopic properties of ammonium sulfate and sodium chloride aerosol at relative humidities approaching saturation., *J. Phys. Chem. A*, 2010, **114**, 12682–12691.

31 B. J. Mason, S.-J. King, R. E. H. Miles, K. M. Manfred, A. M. J. Rickards, J. Kim, J. P. Reid and A. J. Orr-Ewing, Comparison of the accuracy of aerosol refractive index measurements from single particle and ensemble techniques., *J. Phys. Chem. A*, 2012, **116**, 8547–56.

32 T. C. Preston and J. P. Reid, Determining the size and refractive index of microspheres using the mode assignments from Mie resonances, *J. Opt. Soc. Am. A*,

2015, **32**, 2210–2217.

33 N.-O. A. Kwamena, J. Buajarern and J. P. Reid, Equilibrium morphology of mixed organic/inorganic/aqueous aerosol droplets: investigating the effect of relative humidity and surfactants., *J. Phys. Chem. A*, 2010, **114**, 5787–95.

34 R. E. O'Brien, B. Wang, S. T. Kelly, N. Lundt, Y. You, A. K. Bertram, S. R. Leone, A. Laskin, M. K. Gilles, R. E. O'Brien, B. Wang, S. T. Kelly, N. Lundt, Y. You, A. K. Bertram, S. R. Leone, A. Laskin and M. K. Gilles, Liquid–Liquid Phase Separation in Aerosol Particles: Imaging at the Nanometer Scale, *Environ. Sci. Technol.*, 2015, **49**, 4995–5002.

35 Y. You, M. L. Smith, M. Song, S. T. Martin and A. K. Bertram, Liquid–liquid phase separation in atmospherically relevant particles consisting of organic species and inorganic salts, *Int. Rev. Phys. Chem.*, 2014, **33**, 43–77.

36 M. Shiraiwa, A. Zuend, A. K. Bertram and J. H. Seinfeld, Gas-particle partitioning of atmospheric aerosols: interplay of physical state, non-ideal mixing and morphology., *Phys. Chem. Chem. Phys.*, 2013, **15**, 11441–53.

37 L. Renbaum-Wolff, M. Song, C. Marcolli, Y. Zhang, P. F. Liu, J. W. Grayson, F. M. Geiger, S. T. Martin and A. K. Bertram, Observations and implications of liquid–liquid phase separation at high relative humidities in secondary organic material produced by *a*-pinene ozonolysis without inorganic salts, *Atmos. Chem. Phys.*, 2016, **16**, 7969–7979.

38 U. K. Krieger, C. Marcolli and J. P. Reid, Exploring the complexity of aerosol particle properties and processes using single particle techniques, *Chem. Soc. Rev.*, 2012, **41**, 6631.

39 D. J. Stewart, C. Cai, J. Nayler, T. C. Preston, J. P. Reid, U. K. Krieger, C. Marcolli and Y.-H. H. Zhang, Liquid–Liquid Phase Separation in Mixed Organic/Inorganic Single Aqueous Aerosol Droplets, *J. Phys. Chem. A*, 2015, **119**, 4177–4190.

644 40 D. J. Stewart, C. Cai, J. Nayler, T. C. Preston, J. P. Reid, U. K. Krieger, C. Marcolli
645 and Y. H. Zhang, Liquid–Liquid Phase Separation in Mixed Organic/Inorganic
646 Single Aqueous Aerosol Droplets, *J. Phys. Chem. A*, 2015, **119**, 4177–4190.

647 41 A. Zuend and J. H. Seinfeld, A practical method for the calculation of liquid-liquid
648 equilibria in multicomponent organic-water-electrolyte systems using
649 physicochemical constraints, *Fluid Phase Equilib.*, 2013, **337**, 201–213.

650 42 J. Ovadnevaite, A. Zuend, A. Laaksonen, K. J. Sanchez, G. Roberts, D. Ceburnis, S.
651 Decesari, M. Rinaldi, N. Hodas, M. C. Facchini, J. H. Seinfeld and C. O' Dowd,
652 Surface tension prevails over solute effect in organic-influenced cloud droplet
653 activation, *Nature*, 2017, **546**, 637–641.

654 43 A. Zuend and J. H. Seinfeld, Modeling the gas-particle partitioning of secondary
655 organic aerosol: The importance of liquid-liquid phase separation, *Atmos. Chem.*
656 *Phys.*, 2012, **12**, 3857–3882.

657 44 A. Zuend, C. Marcolli, A. M. Booth, D. M. Lienhard, V. Soonsin, U. K. Krieger, D.
658 O. Topping, G. McFiggans, T. Peter and J. H. Seinfeld, New and extended
659 parameterization of the thermodynamic model AIOMFAC: Calculation of activity
660 coefficients for organic-inorganic mixtures containing carboxyl, hydroxyl,
661 carbonyl, ether, ester, alkenyl, alkyl, and aromatic functional groups, *Atmos. Chem.*
662 *Phys.*, 2011, **11**, 9155–9206.

663 45 A. K. Ray and R. Nandakumar, Simultaneous determination of size and
664 wavelength-dependent refractive indices of thin-layered droplets from optical
665 resonances., *Appl. Opt.*, 1995, **34**, 7759–7770.

666 46 O. B. Toon and T. P. Ackerman, Algorithms for the calculation of scattering by
667 stratified spheres, *Appl. Opt.*, 1981, **20**, 3657–3660.

668 47 J. B. Snow, S. X. Qian and R. K. Chang, Stimulated Raman scattering from
669 individual water and ethanol droplets at morphology-dependent resonances., *Opt.*

Lett., 1985, **10**, 37–39.

48 J. Popp, M. Lankers, K. Schaschek, W. Kiefer and J. T. Hodges, Observation of sudden temperature jumps in optically levitated microdroplets due to morphology-dependent input resonances., *Appl. Opt.*, 1995, **34**, 2380–6.

49 J. F. Owen, P. W. Barber, B. J. Messinger and R. K. Chang, Determination of optical-fiber diameter from resonances in the elastic scattering spectrum, *Opt. Lett.*, 1981, **6**, 272.

50 V. S. Ilchenko, A. a Savchenkov, A. B. Matsko and L. Maleki, Dispersion compensation in whispering gallery modes, *J. Opt. Soc. Am. A*, 2003, **20**, 157–162.

51 S. C. Hill, C. K. Rushforth, R. E. Benner and P. R. Conwell, Sizing dielectric spheres and cylinders by aligning measured and computed resonance locations: algorithm for multiple orders, *Appl. Opt.*, 1985, **24**, 2380.

52 R. L. Hightower and C. B. Richardson, Resonant Mie scattering from a layered sphere., *Appl. Opt.*, 1988, **27**, 4850–5.

53 C. F. Bohren and D. R. Huffman, *Absorption and Scattering of Light by Small Particles*, Wiley-VCH Verlag GmbH, Weinheim, Germany, 1998.

54 P. R. Conwell, C. K. Rushforth, R. E. Benner and S. C. Hill, Efficient automated algorithm for the sizing of dielectric microspheres using the resonance spectrum, *J. Opt. Soc. Am. A*, 1984, **1**, 1181.

55 G. P. Dubey, N. Tripathi and S. C. Bhatia, Refractive index of ternary liquid systems of squalane (+ hexane + benzene; + cyclohexane + benzene and + hexane + cyclohexane), *Indian J. Pure Appl. Phys.*, 2005, **43**, 175–179.

56 Haynes W. M., *CRC Handbook of Chemistry and Physics, 97th Edition*, 2017.

57 D. J. Losey, R. G. Parker and M. A. Freedman, pH Dependence of Liquid–Liquid

694 Phase Separation in Organic Aerosol, *J. Phys. Chem. Lett.*, 2016, **7**, 3861–3865.

695